

Drift wave instability in the Helimak experiment

Jean C. Perez and W. Horton

Institute for Fusion Studies, University of Texas at Austin, Austin, Texas 78712-0264

K. Gentle, W. L. Rowan, and K. Lee

Fusion Research Center, University of Texas at Austin, Austin, Texas 78712-0264

Russell B. Dahlburg

Naval Research Laboratory, Code 6440, Washington, D.C. 20375-5344

(Received 1 July 2005; accepted 3 January 2006; published online 10 March 2006)

Electrostatic drift wave linear stability analysis is carried out for the Helimak configuration and compared against experimental data. Density fluctuation and cross-spectrum measurements show evidence of a coherent mode propagating perpendicular to the magnetic field which becomes unstable at $k_{\perp}\rho_s \sim 0.15$. By comparing the experimental results with the wave characteristic of linear two-fluid theory, this mode is identified as an unstable resistive drift wave driven by the density gradient and magnetic grad- B /curvature present in an otherwise magnetohydrodynamic stable steady-state equilibrium. © 2006 American Institute of Physics. [DOI: 10.1063/1.2168401]

I. INTRODUCTION

Drift waves were originally discovered by D'Angelo and Motley (see Ref. 1) and Chen (see Refs. 2–5); their properties were documented in detail by Hendel *et al.* in Q -machine plasmas, as given in Ref. 6. The first detailed explanation of the nonlinear oscillations measured by Hendel experiments is given by Hinton and Horton in Ref. 7. In that reference, the square of the density gradient drives the growth rate through the electron resistivity and parallel thermal diffusivity in a hot ion plasma ($T_i > T_e$) where ion collisional viscosity governs the damping. From these drift wave experiments it became clear that the Bohm diffusion (see Ref. 8) was produced by the large $\mathbf{E} \times \mathbf{B}$ convection in the drift waves driven by the plasma density gradients.

The drift wave instability plays a key role in the turbulent transport of magnetized fusion plasmas, which makes the literature on this subject very extensive. For a review see, for instance, Ref. 9 and references there in. This instability, sometimes called universal instability, is present in most fusion plasmas due to the necessary presence of density and temperature gradients in confined plasmas. However, the experimental study of drift wave instabilities and the associated turbulence and turbulent transport are not simple problems. This difficulty comes from the fact that in order to obtain good plasma confinement a complex toroidal magnetic geometry is necessary. In addition, a complete experimental description of the fluctuations is not always possible either because of the very high temperatures of fusion-grade plasmas or access limitations due to configurational constraints in the confinement devices.

The Helimak is one of a class of basic plasma experiments which manifests selected characteristics of a fusion plasma in a simpler geometry and with better diagnostics than are possible in major confinement devices. The Helimak is a finite realization of the one-dimensional, cylindrical, sheared slab often used in theoretical calculations of plasma turbulence. This correspondence makes possible the com-

parison of well-understood theoretical and numerical models with experimental data. The additions of magnetic curvature and shear are the minimal additions to the ideal slab model required to introduce the effects of a confinement geometry. The field curvature generates a charge-dependent drift of the guiding centers which separates electrons from ions. This charge separation is also mathematically equivalent to the one that occurs from the gravitational field on the surface of the sun. Thus, the experiment can simulate the Rayleigh-Taylor instability in certain regimes. The Helimak is a toroidal device with a cross section shown in Fig. 1. The dominant toroidal field (B_{ϕ}) is of order 0.1 T with a weaker vertical field (B_z) which may be varied up to 10% of the toroidal field. The field lines are thus helices as shown spiraling from bottom to top. The field line length may be varied from less than 20 m to more than 1 km. The height of the vacuum vessel is $L_z = 2H = 2$ m, the inner radius is 0.6 m, and the outer radius 1.6 m. For most conditions, all the field lines terminate at both ends on sets of plates as shown. There are two sets top and bottom, 180° apart. (For the steepest pitches, some field lines terminate on the vessel.) Although each plate is electrically isolated, all are connected to the vacuum vessel in these experiments. The field lines impinge nearly normal to the plates, which are dotted with more than 700 surface-mounted Langmuir probes. The inset illustrates one probe tip with its ceramic insulator protruding through the plate into the plasma. The plasma is formed and heated by up to 6 kW of microwave power at the electron cyclotron frequency. The power is admitted through an open waveguide on the high field side. Since the single-pass absorption is small in this experiment, the vacuum chamber forms a highly overmoded, low- Q cavity—a microwave oven. In argon at a neutral density of 4×10^{11} cm⁻³, typical plasma parameters are $n_e = 10^{11}$ cm⁻³, $T_e = 10$ eV, and $T_i < 0.1$ eV. The full set of parameters is listed in Table I. This configuration has a simple stable magnetohydrodynamic (MHD) equilibrium (see Refs. 10–12) in which the charge separation from vertical drifts is largely neutralized by a return j_{\parallel} and the

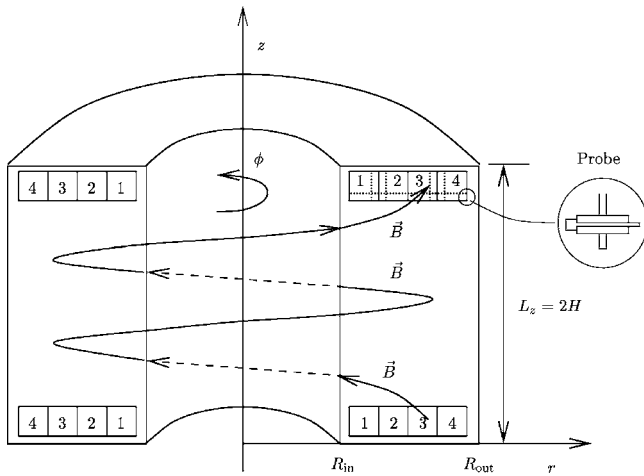


FIG. 1. Helimak cross section showing the magnetic field lines and probe geometry. Four sets of four conducting plates contain over 700 Langmuir probes as shown. Plates are isolated from each other and can be independently biased; however, in this experiment all of them are connected to the vessel.

small j_{\perp} required for force balance flows to the end plates and returns through the conducting vessel. The configuration has been used in other experiments like in Ref. 13 and 14. The latter experiment also uses microwave power for plasma production and reports plasmas with similar equilibrium parameters. This experiment differs from those principally in size, having dimensions large compared with all scale lengths, including those for density and temperature gradients. This experiment operates in a steady state with stationary conditions for tens of seconds, giving excellent statistics for turbulence. It is a full realization of the cylindrical sheared slab.

The heated plasma flows along the field lines, establishing a pressure profile with $\mathbf{B} \cdot \nabla p_e = 0$ on the time scale H/c_s forming nested cylindrical surfaces of constant pressure.

In the viscous-resistive MHD description of the system, the diamagnetic drift frequency $\omega_s \approx k_z v_{de}$ is taken as negligible compared with the larger of the MHD frequency ω^{MHD}

given by $k_{\parallel} v_A$ and the plasma Rayleigh-Taylor growth rate γ^{MHD} . In the MHD regime, one can show that the Ohm's law is

$$E_{\parallel} + \frac{\nabla_{\parallel} p_e}{en} \approx E_{\parallel} = \eta j_{\parallel}. \quad (1)$$

The resistive MHD modes are analyzed in detail in Dahlburg *et al.*¹⁵ For the weaker drift wave instabilities the situation is reversed in Eq. (1), with

$$E_{\parallel} \approx -\frac{\nabla p_e}{en_e} \approx -\frac{T_e}{en_e} \nabla_{\parallel} n_e \quad (2)$$

being the balance in the Ohm's law. One can see that for the lower frequencies of drift waves $\delta n_e/n_e \sim e \delta \phi / T_e$, whereas for a MHD instability driven by the sheared mass flows $\gamma \sim |dv_z/dr| > \omega_{*e}$ the density fluctuations are small with $e \delta \phi / T_e \gg \delta n_e/n_e$. Here, we derive the electric field from the electric potential ϕ with

$$E_{\parallel} = -\nabla_{\parallel} \phi. \quad (3)$$

The regime of Eq. (2) is called the adiabatic regime, since

$$\delta n_e = n_e e^{e \delta \phi / T_e} \approx n_e \left(1 + \frac{e \delta \phi}{T_e} \right) \quad (4)$$

along the magnetic field line. In the following we describe strongly driven flow drift wave linear instabilities derived from a two-fluid approach, using Fourier decomposition of the fluctuating quantities along the ϕ and z coordinates with wave numbers $k_{\phi} = l/r$ ($l=0, 1, \dots$) and $k_z = m\pi/L_z$ ($m=0, 1, \dots$), where $L_z = 2H$ is the height of the Helimak chamber. The fluctuating density and electrostatic potential thus vary as the real parts of $[\delta n(r), \delta \phi(r)] \exp(-i\omega t - il\phi + ik_z z)$.

This paper is organized as follows. Section II is devoted to the description of the Helimak equilibrium with measurements of radial equilibrium profiles shown. In Sec. III we perform the linear stability analysis of the Helimak plasma within the framework of two-fluid theory. In Sec. IV we present recent experimental data which shows measurements and characterization of the density fluctuations. In Sec. V we conclude.

TABLE I. Helimak important typical plasma parameters.

Electron gyrofrequency	$f_{ce} = 2.80 \times 10^9$ Hz
Ion gyrofrequency	$f_{ci} = 3.80 \times 10^4$ Hz
Electron plasma frequency	$f_{pe} = 2.84 \times 10^9$ Hz
Ion plasma frequency	$f_{pi} = 1.05 \times 10^7$ Hz
Electron collision rate	$\nu_e = 1.31 \times 10^5$ s ⁻¹
Ion collision rate	$\nu_i = 2.08 \times 10^6$ s ⁻¹
Debye length	$\lambda_D = 7.43 \times 10^{-3}$ cm
Electron gyroradius	$\rho_e = 7.53 \times 10^{-3}$ cm
Ion gyroradius	$\rho_i = 1.12 \times 10^{-1}$ cm
Ion-acoustic gyroradius	$\rho_s = 2.05$ cm
Electron thermal velocity	$v_{Te} = 1.32 \times 10^8$ cm/s
Ion thermal velocity	$v_{Ti} = 2.68 \times 10^4$ cm/s
Ion sound velocity	$c_s = 4.9 \times 10^5$ cm/s
Alfvén velocity	$v_A = 1.09 \times 10^8$ cm/s
Electric drift velocity	$v_E = 1.50 \times 10^6$ cm/s

II. HELIMAK EQUILIBRIUM

For the Helimak configuration described in the previous section, a MHD stable equilibrium exists as extensively described in Ref. 12. We will present the most important results of this reference regarding the MHD equilibria on which we operate in the reported experiment.

It is generally well known that in a purely toroidal magnetic field no MHD equilibria exists. The charge-dependent magnetic curvature drift and gradient drift give rise to a charge separation that can quickly establish large vertical electric field producing radial $\mathbf{E} \times \mathbf{B}$ plasma flows toward the wall. However, in the Helimak there is a small but finite vertical magnetic field component that allows for a vertical current shorting out the polarization fields due to the gradient B drift. This vertical current finds its closed path on the inner

and outer conducting walls of the vacuum chamber. There is a small vertical current that makes possible the Helimak MHD equilibria.

As a first approximation we model the Helimak to be uniform along the vertical direction with standing mode boundary conditions at the top and bottom plates. Then, we assume the equilibrium has $\partial/\partial\phi = \partial/\partial z = 0$ and the equilibrium fields are

$$p = p(r), \quad (5)$$

$$\rho = \rho(r), \quad (6)$$

$$\mathbf{v} = v_\phi(r)\mathbf{e}_\phi + v_z(r)\mathbf{e}_z, \quad (7)$$

$$\mathbf{B} = B_\phi(r)\mathbf{e}_\phi + B_z(r)\mathbf{e}_z. \quad (8)$$

The force balance equation takes the form

$$\frac{d}{dr} \left(p + \frac{B_z^2}{2\mu_0} \right) + \frac{\mu_0 I_z}{4\pi r^2} \frac{dI_z}{dr} - \frac{\rho v_\phi^2}{r} = 0, \quad (9)$$

where $\mu_0 I_z(r) = 2\pi r B_\phi$.

The linear ideal MHD stability of this equilibrium, given by Luckhardt,¹² leads to the local Suydam criterion with the magnetic shear $k_{\parallel} = k_z(r - r_s)/L_s$,

$$\frac{2\mu_0 p'(r)}{B_z^2(r)} + \frac{r}{4} \left[\frac{q'(r)}{q(r)} \right]^2 \Big|_{r=r_s} > 0 \quad (10)$$

near the resonant surface $r = r_s$, defined as the surfaces for which the helical mode (l, m) follows the pitch of the magnetic field. Here, q is equivalent to the tokamak safety factor $q(r) = HB_\phi/\pi r B_z$. The shear length L_s defined through the local k_{\parallel} is $1/L_s = 2B_z/rB_\phi$, while the connection length is given by $L_c = 2HB/B_z$.

The current $I_z = I_z^{\text{ext}} + \Delta I_p$ in Ampère's law $2\pi r B_\phi = \mu_0 I_z(r)$ is composed of the external current provided by the poloidal coils I_z^{ext} and the induced plasma current ΔI_p . The current $\Delta I_p \sim 100$ A can be neglected when compared to the external one of $I_z \sim 10$ kA. Thus, in the rest of the paper we use the vacuum magnetic field as the dominant field in the Helimak, so that the MHD stability criterion becomes $\beta_p = 2\mu_0 \langle p \rangle / B_z^2 < L_p / r_0 \sim 0.1$, where $L_p = -(dp/dr)/p$ is the pressure gradient scale length and $r_0 \sim 1$ m is the radius at which the pressure profile peaks.

The pressure profile is given by the measured electron densities from swept probe I - V characteristics from a radial probe array of 80 probes. The electron temperature is fairly uniform throughout the plasma due to the fast electron thermal conductivity. Typical radial equilibrium density, electron temperature, and floating potential profiles at the position $z = -74$ cm from the midplane are shown in Fig. 2. Measured profiles at the top and bottom ends of the machine, $z = +74$ cm and $z = -74$ cm, respectively, are the same within less than 5%, indicating uniformity of the equilibrium properties on both sides of the $z = 0$ cm midplane.

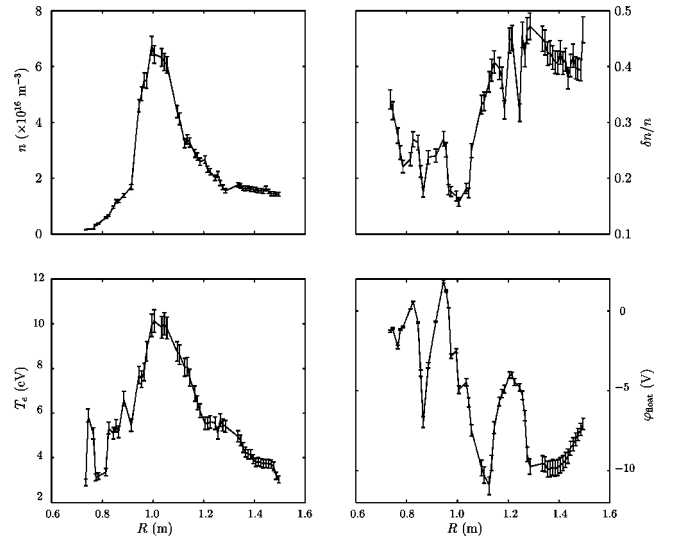


FIG. 2. The Helimak operates in a steady state with a duration of 30 s. Radial equilibrium density, electron temperature, and floating potential profiles are shown. All profiles are measured as a function of radius by Langmuir probes spanning the vessel. Also shown is a radial profile of the density fluctuation level, $\delta n/n$, measured by probes collecting ion saturation current. Distance is measured from the central vertical axis of the torus.

III. DRIFT WAVE INSTABILITY

We present the linear analysis of low-frequency electron drift waves from the Braginskii¹⁶ two-fluid description that considers separate dynamics for each plasma species,

$$m_s n_s \frac{d}{dt} \mathbf{v}_s = -\nabla p_s + e_s n_s (\mathbf{E} + \mathbf{v}_s \times \mathbf{B}) + \mathbf{R}_s, \quad s = \{e, i\}, \quad (11)$$

where \mathbf{R}_s is the friction force between species, assumed to be parallel to the magnetic field

$$\mathbf{R}_e = m_e n_e \nu_e (\mathbf{v}_{\text{ill}} - \mathbf{v}_{\text{ell}}) \hat{\mathbf{b}} \quad \text{with} \quad \hat{\mathbf{b}} \equiv \frac{\mathbf{B}}{B}, \quad (12)$$

$$\mathbf{R}_i = -\mathbf{R}_e, \quad (13)$$

where ν_e is the electron-ion collision rate. The perpendicular dynamics can be obtained by crossing (11) with the magnetic field

$$\begin{aligned} \mathbf{v}_{s\perp} &= \frac{\mathbf{E} \times \mathbf{B}}{B^2} + \frac{\hat{\mathbf{b}}}{\Omega_s} \times \left[\frac{\nabla p_s}{m_s n_s} + \left(\frac{\partial}{\partial t} + \mathbf{v}_s \cdot \nabla \right) \mathbf{v}_s \right] \\ &= \mathbf{v}_E + \mathbf{v}_{ds} + \frac{\hat{\mathbf{b}}}{\Omega_s} \times \left(\frac{\partial}{\partial t} + \mathbf{v}_s \cdot \nabla \right) \mathbf{v}_s, \end{aligned} \quad (14)$$

with $\mathbf{v}_E = \mathbf{E} \times \mathbf{B} / B^2$, $\mathbf{v}_{ds} = \hat{\mathbf{b}} \times \nabla p_s / e_s B n_s$, and $\Omega_s \equiv e_s B / m_s$ being the $\mathbf{E} \times \mathbf{B}$ drift, the diamagnetic drift, and the gyrofrequency of species s , respectively. Expression (14) contains the drifts associated with each plasma species $s = i, e$. In the drift ordering, the small parameter $\epsilon = \rho_s / L_\perp$ is used as an expansion parameter, in which $\rho_s = c_s / \Omega_s$ is the ion-acoustic scale length and c_s the ion sound speed. It is also further assumed that

$$\frac{\mathbf{v}_E}{c_s} \sim \frac{\mathbf{v}_d}{c_s} \sim \frac{1}{\Omega_i} \frac{\partial}{\partial t} \sim \epsilon. \quad (15)$$

Hence, the perpendicular drift-ordered flow velocity is

$$\mathbf{v}_{s\perp} = \mathbf{v}_E + \mathbf{v}_{ds} + O(\epsilon^2). \quad (16)$$

As is well known, the first drift does not lead to a perpendicular current in the plasma as long as quasineutrality can be maintained. The second drift is due to the existence of the equilibrium pressure gradient. This drift, being in opposite directions for ion and electrons, gives rise to a diamagnetic current that provides the equilibrium force balance $\nabla p = \mathbf{j} \times \mathbf{B}$.

By recursively solving Eq. (14), we obtain the polarization drift

$$\mathbf{v}_{ps} = \frac{m_s}{e_s B} \hat{\mathbf{b}} \times \left(\frac{\partial}{\partial t} + \mathbf{v}_E \cdot \nabla \right) (\mathbf{v}_E + \mathbf{v}_{ds}), \quad (17)$$

which is second order in ϵ . Diamagnetic cancellation¹⁷ is included in the last equation after taking the $\mathbf{E} \times \mathbf{B}$ flow as the only advecting flow. Due to the large mass ratio, the polarization drift is dominated by ions so that we can neglect the inertia term in the electron drifts; consequently, we have that $\mathbf{v}_{pe} \approx 0$.

Although the polarization drift is second order in ϵ , it is important to retain it because its contribution to charge conservation determines the evolution of the electrostatic potential and helps maintain quasineutrality. Hence, for cold ions the polarization current is given by

$$\mathbf{j}_p = \frac{en_i}{\Omega_i} \hat{\mathbf{b}} \times \frac{d}{dt} \mathbf{v}_E = \frac{en_i}{\Omega_i} \frac{d}{dt} \left(\frac{\mathbf{E}_\perp}{B} \right) = - \frac{m_i n_i}{B^2} \frac{d}{dt} \nabla \varphi(\mathbf{x}, t) \quad (18)$$

for electrostatic fluctuations.

Another contribution to the perpendicular current comes from the electron diamagnetic drift,

$$\mathbf{j}_d = -ne\mathbf{v}_{de} = \frac{\hat{\mathbf{b}} \times \nabla p_e}{B}. \quad (19)$$

Up to now we have used the perpendicular part of the electron and ion fluid dynamics to obtain the relevant drifts for the Helimak typical operating conditions.

The parallel dynamics for the electrons gives the constitutive relation for isothermal electrons,

$$E_\parallel + \frac{\nabla_\parallel p_e}{en_e} = \eta j_\parallel \Rightarrow -\nabla_\parallel \varphi + \frac{T_e \nabla_\parallel n_e}{en_e} = \eta j_\parallel, \quad (20)$$

which couples the electrostatic potential and the density through the parallel current j_\parallel . In the next section we will obtain the dynamic equations for φ and $n_e = n_i = n$ from quasineutrality and particle conservation.

A. Quasineutrality

In the preceding section, we obtained the total current in the drift ordering

$$\mathbf{j} = \mathbf{j}_p + \mathbf{j}_d + j_\parallel \hat{\mathbf{b}} \quad (21)$$

made of fluid drifts across the magnetic field and a parallel current arising from the free-electron streaming along the ambient magnetic field. For a quasineutral state, charge conservation gives the potential evolution equation

$$\nabla \cdot \mathbf{j} = \nabla \cdot \mathbf{j}_p + \nabla \cdot \mathbf{j}_d + \nabla_\parallel j_\parallel = 0. \quad (22)$$

The contribution to the continuity equation from each current is given by

$$\nabla \cdot \mathbf{j}_p = -\nabla_\perp \cdot \left[\frac{m_i n}{B^2} \frac{d}{dt} \nabla_\perp \varphi \right], \quad (23)$$

$$\nabla \cdot \mathbf{j}_d = -2\mathbf{j}_d \cdot \nabla \ln B. \quad (24)$$

Quasineutrality then gives

$$-\frac{m_i n}{B^2} \frac{d}{dt} \nabla_\perp^2 \varphi - 2\mathbf{j}_d \cdot \nabla \ln B + \nabla_\parallel j_\parallel = 0 \quad (25)$$

from Eqs. (22)–(24), where we reduce the term $\nabla_\perp \cdot \mathbf{j}_p$ with $\nabla_\perp \ln \varphi = ik_\perp \varphi \gg \nabla_\perp \ln n$.

The evolution of the number density $n_e = n_i = n$ is given by the continuity equation

$$\frac{\partial n}{\partial t} + \mathbf{v}_E \cdot \nabla n + n \nabla_\perp \cdot \mathbf{v}_E + \nabla \cdot (n \mathbf{v}_{de}) + \nabla_\parallel (n v_{e\parallel}) = 0. \quad (26)$$

The equivalent analysis for the tokamak geometry is more complicated due to the internal plasma current and the periodic variation of the magnetic curvature as shown in Ref. 18.

Notice that in Eq. (26) we are ignoring plasma sources and sinks which are present in the Helimak. This effect can be modeled by including the two new terms $C - \alpha n^2$ on the right-hand side of the continuity equation. Here, C is the ionization rate and αn^2 is the recombination rate at 10 eV. However, for the frequencies of interest in this work, this loss rate given by α is a small shift of the growth rates downward (by $2\alpha n$) from their $\alpha=0$ values.

The compression of the $\mathbf{E} \times \mathbf{B}$ flow, due to magnetic curvature, is

$$\nabla \cdot \mathbf{v}_E = -2\mathbf{v}_E \cdot \nabla \ln B, \quad (27)$$

so that the evolution for the density is determined by the equation

$$\frac{\partial n}{\partial t} + \mathbf{v}_E \cdot \nabla n - 2n(\mathbf{v}_E + \mathbf{v}_{de}) \cdot \nabla \ln B + \nabla_\parallel (n v_{e\parallel}) = 0. \quad (28)$$

Equations (25) and (28) constitute the full nonlinear model we use to describe fluctuations of φ, n in this work. As can be seen, this model reduces to the Hasegawa-Wakatani¹⁹ model in the absence of magnetic gradient and curvature.

B. Linear analysis and parallel Ohm's law

Now, we turn to the determination of the parallel current in terms of the fields φ, n from the parallel dynamics for electrons and ions. The parallel current in the plasma is given by $j_\parallel = en(v_{i\parallel} - v_{e\parallel})$, where $v_{e\parallel}$ and $v_{i\parallel}$ can be obtained from the parallel momentum equation for each species in the direction parallel to the magnetic field.

For electrons, neglecting the mass in the momentum balance equation (11), we get

$$-en\nabla_{\parallel}\varphi + T_e\nabla_{\parallel}n = m_e n v_e(v_{i\parallel} - v_{e\parallel}), \quad (29)$$

while for ions

$$m_i \frac{d}{dt} v_{i\parallel} = eE_{\parallel}. \quad (30)$$

Consider an equilibrium state $\varphi_0(r)$, $n_0(r)$, $v_{e\parallel}^{(0)}$, $v_{i\parallel}^{(0)}$ such that

$$\nabla_{\parallel}\varphi_0 = 0; \quad \nabla_{\parallel}n_0 = 0; \quad v_{e\parallel}^{(0)} = 0; \quad v_{i\parallel}^{(0)} = 0, \quad (31)$$

with the magnetic field of the form given by (8) and make small perturbations around this equilibrium,

$$\varphi(r, \phi, z, t) = \varphi_0(r) + \delta\varphi(r, \phi, z, t), \quad (32)$$

$$n(r, \phi, z, t) = n_0(r) + \delta n(r, \phi, z, t), \quad (33)$$

$$v_{e\parallel}(r, \phi, z, t) = \delta v_{e\parallel}(r, \phi, z, t), \quad (34)$$

$$v_{i\parallel}(r, \phi, z, t) = \delta v_{i\parallel}(r, \phi, z, t). \quad (35)$$

Equation (29) then becomes

$$en_0\nabla_{\parallel}\delta\varphi - T_e\nabla_{\parallel}\delta n = \frac{m_e v_e}{e} j_{\parallel}, \quad (36)$$

where

$$\nabla_{\parallel} = \hat{\mathbf{b}} \cdot \nabla; \quad \hat{\mathbf{b}} \equiv \frac{\mathbf{B}}{B}. \quad (37)$$

The fluctuation fields δf are taken to be of the form $\delta f(r, \phi, z, t) = \delta f(r) e^{-i\omega t - i\ell\phi + ik_z z} + \text{c.c.}$. The derivative of the fluctuations along the unperturbed equilibrium magnetic field is

$$\mathbf{b} \cdot \nabla \equiv \nabla_{\parallel} \equiv ik_{\parallel} = i \left(\frac{k_z B_z}{B} - \frac{\ell B_{\phi}}{rB} \right). \quad (38)$$

It is useful to define a perpendicular wave vector \mathbf{k}_{\perp} which is perpendicular to both \mathbf{B} and $\hat{\mathbf{e}}_r$. This leads to

$$\nabla_{\perp} \equiv \hat{\mathbf{e}}_r \frac{d}{dr} + i\mathbf{k}_{\perp} = \hat{\mathbf{e}}_r \frac{d}{dr} - i \left(\frac{\ell B_z}{rB} + \frac{k_z B_{\phi}}{B} \right) \mathbf{n}, \quad (39)$$

where $\mathbf{n} = \mathbf{b} \times \hat{\mathbf{e}}_r$. Notice that for low magnetic field pitches or axisymmetric modes, the perpendicular wave vector is $k_{\perp} \approx k_z$, rather than k_y , as is usually the case in toroidal magnetic confinement geometries.

With these definitions we have that, when acting on fluctuating quantities,

$$\nabla = \hat{\mathbf{e}}_r \frac{d}{dr} + i\mathbf{k}_{\perp} + ik_{\parallel}, \quad (40)$$

so that Eq. (36) becomes

$$\frac{j_{\parallel}}{n_0 e} = ik_{\parallel} D_{\parallel} \left(\frac{\delta n}{n_0} - \frac{e\delta\varphi}{T_e} \right), \quad (41)$$

with $D_{\parallel} \equiv T_e/m_e v_e$. In the absence of electron collisions, this equation becomes the Boltzmann's relation for adiabatic

electrons. Another equation relating the fluctuating fields δn , $\delta\varphi$, and $\delta v_{e\parallel}$ is obtained by linearizing the continuity equation (28),

$$-i\omega\delta n + \mathbf{v}_E^{(0)} \cdot \nabla_{\perp} \delta n + \delta\mathbf{v}_E \cdot \nabla_{\perp} n_0 - 2n_0(\delta\mathbf{v}_E + \delta\mathbf{v}_{de}) \cdot \nabla \ln B + ik_{\parallel} n_0 \delta v_{e\parallel} = 0, \quad (42)$$

with

$$\mathbf{v}_E^{(0)} = \frac{\hat{\mathbf{b}} \times \nabla \varphi_0}{B}, \quad \delta\mathbf{v}_E = \frac{\hat{\mathbf{b}} \times \nabla \delta\varphi}{B},$$

$$\delta\mathbf{v}_{de} = -\frac{T_e \hat{\mathbf{b}} \times \nabla \delta n}{eBn_0}. \quad (43)$$

Collecting the results for the terms in Eq. (42),

$$\mathbf{v}_E^{(0)} \cdot \nabla_{\perp} \delta n = i\mathbf{v}_E^{(0)} \cdot \mathbf{k}_{\perp} \delta n, \quad (44)$$

$$\delta\mathbf{v}_E \cdot \nabla_{\perp} n_0 = -\frac{ik_{\perp}}{B} \frac{dn_0}{dr} \delta\varphi, \quad (45)$$

$$\delta\mathbf{v}_E \cdot \nabla \ln B = \frac{ik_{\perp}}{R_c B} \delta\varphi, \quad (46)$$

$$\delta\mathbf{v}_{de} \cdot \nabla \ln B = -\frac{ik_{\perp} T_e}{eBR_c n_0} \delta n. \quad (47)$$

In Eqs. (46) and (47), $R_c = -B/(dB/dr) = r$ is the local radius of curvature of the magnetic field line and r is the radius measured from the central vertical axis of the Helimak. The linear electron continuity equation (42) gives the relation

$$\frac{\delta n}{n_0} = \frac{1}{\tilde{\omega}} \left[(\omega_* - \omega_D) \frac{e\delta\varphi}{T_e} + \omega_D \frac{\delta n}{n_0} + k_{\parallel} \delta v_{i\parallel} - k_{\parallel} \frac{j_{\parallel}}{n_0 e} \right]. \quad (48)$$

We use the Doppler-shifted frequency in the plasma frame

$$\tilde{\omega} = \omega - \mathbf{k}_{\perp} \cdot \mathbf{v}_E^{(0)}, \quad (49)$$

where ω is the frequency in the laboratory frame of reference. When the plasma has an $E_r > 0$, the $v_E = E_r/B_{\phi}$ is opposite to the electron diamagnetic drift on the low field side of the density maximum and parallel to the diamagnetic drift on the high field side.

In Eq. (48) we define the diamagnetic drift frequency ω_* and the grad- B /curvature drift frequency ω_D as

$$\omega_* = k_{\perp} v_d = -k_{\perp} \frac{T_e}{eB} \frac{1}{n_0} \frac{dn_0}{dr} = \frac{k_{\perp} T_e}{eBL_n}, \quad (50)$$

$$\omega_D = -k_{\perp} \frac{2T_e}{eB^2} \frac{dB}{dr} = k_{\perp} \frac{2T_e}{eBR_c}. \quad (51)$$

Interchange unstable (stable) regions have $\omega_* \omega_D > 0$ ($\omega_* \omega_D < 0$), corresponding to $L_n > 0$ on the low field side ($L_n < 0$ on the high field side).

From the ion parallel momentum equation we have

$$-i\tilde{\omega} m_i \delta v_{i\parallel} = eE_{\parallel} \Rightarrow v_{i\parallel} = \frac{k_{\parallel} e \delta\varphi}{m_i \tilde{\omega}}, \quad (52)$$

so that Eq. (48) becomes

$$\frac{\delta n}{n_0} = \frac{1}{\tilde{\omega}} \left[\left(\omega_* - \omega_D + \frac{c_s^2 k_{\parallel}^2}{\tilde{\omega}} \right) \frac{e \delta \varphi}{T_e} + \omega_D \frac{\delta n}{n_0} - k_{\parallel} \frac{j_{\parallel}}{n_0 e} \right]. \quad (53)$$

Now, we use Eq. (41) to eliminate the parallel current j_{\parallel} from Eq. (53) to obtain

$$\frac{\delta n}{n_0} = \frac{\omega_* - \omega_D + k_{\parallel}^2 c_s^2 / \tilde{\omega} + i \nu_{\parallel} e \delta \varphi}{\tilde{\omega} - \omega_D + i \nu_{\parallel} T_e}, \quad (54)$$

with $\nu_{\parallel} \equiv k_{\parallel}^2 D_{\parallel}$. For the Helimak experiments reported in this work the dominant mode frequency is about 1.2 kHz or $\omega \sim 7.5 \times 10^3$ rad/s, and the typical parallel wave vector $k_{\parallel} \sim 10^{-3}$ cm $^{-1}$, so that the condition $\omega \ll \nu_{\parallel}$ holds and we can approximate

$$\frac{\delta n}{n_0} = \left(1 - i \frac{\omega_* - \tilde{\omega} + k_{\parallel}^2 c_s^2 / \tilde{\omega}}{k_{\parallel}^2 D_{\parallel}} \right) \frac{e \delta \varphi}{T_e} \equiv [1 - i \delta(\omega, \mathbf{k})] \frac{e \delta \varphi}{T_e}, \quad (55)$$

in which

$$\delta(\omega, \mathbf{k}) = \frac{\omega_* - \tilde{\omega} + k_{\parallel}^2 c_s^2 / \tilde{\omega}}{k_{\parallel}^2 D_{\parallel}}. \quad (56)$$

In the collisionless regime $\delta=0$, so we recover the Boltzmann relation for adiabatic electrons. Taking kinetic effects into account will lead to a nonvanishing collisionless δ due to wave particle interaction, giving $\delta n/n_0 \approx [1 + i(\pi/2)^{1/2}(\omega - \omega_*)/|k_{\parallel}|v_{Te}]e\varphi/T_e$, and the continuous transition in $\nu_e/|k_{\parallel}|v_{Te}$ requires $\nu_{\parallel} = k_{\parallel}^2 v_{Te}^2 / [\nu_e + (2/\pi)^{1/2}|k_{\parallel}|v_{Te}]$.

In a similar fashion, we can obtain an expression for the divergence of the parallel current

$$\nabla_{\parallel} j_{\parallel} = i k_{\parallel} j_{\parallel} = i e n \frac{\omega_* - \tilde{\omega} + k_{\parallel}^2 c_s^2 / \tilde{\omega} e \delta \tilde{\varphi}}{1 - i(\tilde{\omega} - \omega_D)/\nu_{\parallel} T_e}, \quad (57)$$

which for $\tilde{\omega} - \omega_D \ll \nu_{\parallel}$ becomes

$$\nabla_{\parallel} j_{\parallel} = i k_{\parallel} j_{\parallel} = i e n [\omega_* - \tilde{\omega} + k_{\parallel}^2 c_s^2 / \tilde{\omega} + i(\tilde{\omega} - \omega_D) \delta(\omega, \mathbf{k})] \frac{e \delta \tilde{\varphi}}{T_e}. \quad (58)$$

In the next section we will derive the radial eigenmode equation that determines the radial eigenmodes.

C. Eigenmode equation and dispersion relation

We can now eliminate $\delta n/n$ and j_{\parallel} from Eq. (25) to obtain the linear eigenvalue problem

$$\left[\frac{\rho_s^2}{r} \frac{d}{dr} \left(r \frac{d}{dr} \right) + \lambda + \frac{c_s^2}{\tilde{\omega}^2} k_{\parallel}^2 + i \delta(\omega, \mathbf{k}) \right] \frac{e \delta \varphi}{T_e} = 0, \quad (59)$$

where

$$\rho_s = \frac{c_s}{\Omega}, \quad (60)$$

$$c_s = \sqrt{\frac{T_e}{m_i}}, \quad (61)$$

$$\lambda = -1 - k_{\perp}^2 \rho_s^2 + \frac{\omega_* - \omega_D}{\tilde{\omega}} + \frac{k_{\perp}^2 \rho_s^2}{\tilde{\omega} B} \nabla_{\perp}^2 \varphi_0'(r). \quad (62)$$

In the absence of parallel dissipation ($\delta=0$) and equilibrium $\mathbf{E} \times \mathbf{B}$ sheared flows ($\varphi_0=0$), this equation leads to the local dispersion relation

$$(1 + k_{\perp}^2 \rho_s^2) \tilde{\omega}^2 - (\omega_* - \omega_D) \tilde{\omega} - k_{\parallel}^2 c_s^2 = 0, \quad (63)$$

which can be identified as the usual dispersion relation for drift waves coupled to ion-acoustic modes, modified by the presence of magnetic curvature. These modes can be driven unstable by the parallel dissipation provided through $\delta(\omega, \mathbf{k})$. In this case the dispersion relation is

$$(1 + k_{\perp}^2 \rho_s^2) \tilde{\omega}^2 - (\omega_* - \omega_D) \tilde{\omega} - k_{\parallel}^2 c_s^2 - i \frac{\tilde{\omega}^2 (\omega_* - \tilde{\omega})}{\nu_{\parallel}} = 0, \quad (64)$$

where we neglect contributions from the ion-acoustic mode assuming $k_{\parallel} c_s \ll \tilde{\omega} \ll \nu_{\parallel}$. The dispersion relation reduces to

$$(1 + k_{\perp}^2 \rho_s^2) \tilde{\omega} = \omega_* - \omega_D + i \frac{\tilde{\omega} (\omega_* - \tilde{\omega})}{\nu_{\parallel}}. \quad (65)$$

For large enough ν_{\parallel} the growth rate is given approximately by the formula

$$\gamma_k \approx \frac{\omega_* (\omega_* k_{\perp}^2 \rho_s^2 + \omega_D)}{\nu_{\parallel} (1 + k_{\perp}^2 \rho_s^2)^3}, \quad (66)$$

which has two regimes: For the low $k_{\perp} \rho_s$ values on the low field side (where the parallel diamagnetic and guiding center ∇B drifts give $\omega_* \omega_D > 0$), the growth rate varies as $\gamma_k \approx (\omega_* \omega_D / \nu_{\parallel})$. At high $k_{\perp} \rho_s$ and/or in the high field side (where $\omega_* \omega_D < 0$), the growth rate increases strongly with the mode number $\gamma_k \approx \omega_*^2 (k_{\perp} \rho_s)^2 / \nu_{\parallel}$ until the ion viscosity damping $k_{\perp}^2 \mu = 0.3 \nu_i k_{\perp}^2 \rho_i^2$ brings the growth rate back to zero. The importance of the ion viscous damping is clearly shown in the Hinton and Horton⁷ analysis of the Hendel *et al.* experiments.⁶ For the cylindrical experiments there is no resistive curvature gradient driven drift wave since $\omega_D=0$.

The general shape of the wave dispersion and growth rate is a strong function of the parallel wave number through $\nu_{\parallel} = k_{\parallel}^2 D_{\parallel}$ and $|k_{\parallel}|v_{Te}$ with a complicated transition. We introduce the ratio of linear wave time scales at the short wavelengths $k_z \rho_s = 1$ defined by

$$\hat{\eta} \equiv \frac{|\omega_*|}{\nu_{\parallel}} = \frac{v_d \rho_s}{D_{\parallel}} \left(\frac{B}{B_z} \right)^2, \quad (67)$$

$$\alpha \equiv \sqrt{\frac{2}{\pi}} \frac{|k_{\parallel}| v_{Te}}{\nu_e} = \sqrt{\frac{2}{\pi}} \frac{B_z v_{Te}}{\pi B \nu_e \rho_s}.$$

Estimates of k_{\parallel} together with measurements of v_d and k_z and other plasma parameters give $\hat{\eta} = 1.5$ – 4.5 and $\alpha = 0.24$ – 0.5 . Figure 3 shows how the growth rate depends on the vertical mode number m for a fixed density gradient L_n and radius of curvature $\epsilon_n = 2L_n/R_c$ in the case $\hat{\eta} = 4.5$ and $\alpha = 0.25$. The maximum growth rate $\gamma_{\max} L_n / c_s = 0.31$ in Fig. 3 occurs for $k_{\perp} \rho_s \sim 0.18$, which corresponds to $m = 5$. Figure 3(a) shows

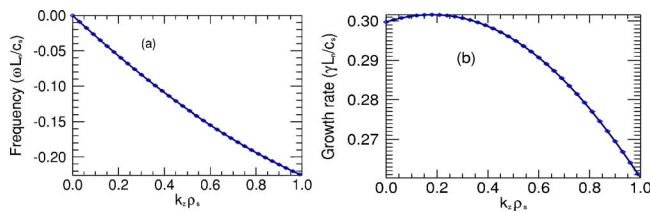


FIG. 3. (a) Frequency spectrum from the quadratic linear dispersion relation. (b) Unstable growth rates as function of $k_{\perp}\rho_s$. The higher frequency root in the left panel is heavily damped and not shown. Each diamond corresponds to integer mode numbers $k_z = m\pi/2H$.

the frequency spectrum in the plasma frame in which the bottom branch corresponds to the unstable growth rates shown in Fig. 3(b). The dimensionless frequency of the most unstable mode corresponds to the physical frequency $\tilde{\omega} = 632$ rad/s.

IV. FLUCTUATION MEASUREMENTS

Original experimental studies of drift waves in nonfusion plasmas are found in Refs. 1–5, although the Helimak experiment is unique in that it possesses both toroidal curvature and magnetic shear. The characteristics of the density fluctuations are investigated as a function of the connection length along the magnetic field lines. An argon discharge is run for a duration of 30 s for each shot, during which both the vertical and toroidal fields as well as the input power from the electron cyclotron resonance heating (ECRH) are kept constant. Between subsequent shots the ratio of the vertical to toroidal field is adjusted so that we are able to scan through the entire range of pitches, corresponding to connection lengths along the field lines from bottom to top end plates between ≈ 10 m and 1 km. A typical probe signal from the low field side (LFS) of the density maximum is shown in Fig. 4. Measured densities from probe I - V characteristics range up to $n \approx 10^{11}$ cm $^{-3}$ with $L_n = -n/(dn/dr) \approx 0.1$ m, while the electron temperature is broad and peaks at $T_e \approx 10$ eV.

Both ion saturation and floating potential fluctuation data are collected by a 16-channel, 14 bit digitizer operated at a sampling rate of 112.5 kSamples/s per channel, providing a Nyquist frequency of 56.25 kHz. The statistics are based on a total number of 1.125×10^6 points culled from 10 s during a stationary period in a 30 s shot. In calculating the spectra

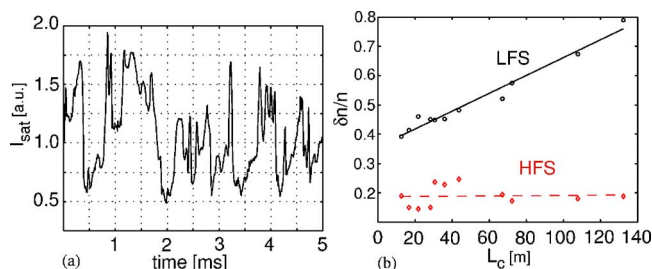


FIG. 4. (a) Sample of time series lasting 5 ms from a probe collecting ion saturation current during a discharge. (b) Measured density fluctuation level amplitude normalized by the mean as a function of the connection length along helical field lines for both the LFS and the HFS.

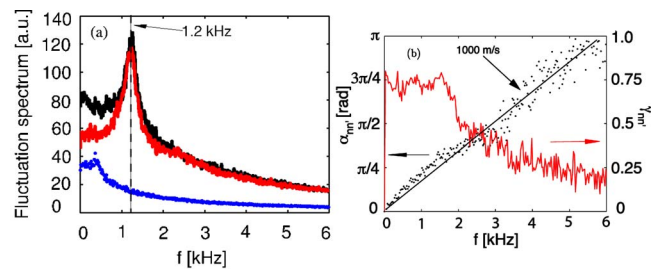


FIG. 5. (a) Frequency spectrum of three probes collecting ion saturation data. The density maximum is located at $r=114$ cm from the vertical axis. The two LFS probes are at $r=122$ cm (solid black) and $r=130$ cm (solid red). The HFS probe is located at $r=101$ cm (dotted blue). (b) Coherency, γ_{nm} , and cross phase, α_{nm} , between two probes separated by a vertical distance of 10 cm, located on the LFS. The slope of α_{nm} gives a phase velocity of 1000 m/s, and its positive sign indicates propagation in the $+z$ direction.

we use 4096 points per autopower spectrum and 2048 points per cross spectrum, giving 275 and 550 realizations, respectively.

Figure 4(b) shows the measurement of the normalized fluctuation amplitude, $\delta n/n$, as a function of the connection length along the field lines. On the LFS we observe that for short connection lengths $\delta n/n$ is $\sim 40\%$, but this quantity increases to well over 50% as the connection length increases, suggesting that overall turbulence levels increase. On the high field side (HFS) the fluctuation amplitude remains around 20% for all values of connection length. Looking at the relative amplitude of the density fluctuations $\delta n/n$ to the potential fluctuations, $e\delta\phi/T_e$, we find that the fluctuation levels are of the same magnitude to within a factor of 2 as expected for drift waves for all connection lengths in the range $20 \text{ m} \leq L_c \leq 50 \text{ m}$ with no apparent increasing or decreasing trend.

Frequency spectra for different probe collecting ion saturation data are shown in Fig. 5(a). The two signals from probes located on the LFS of the density peak display a well-defined peak at $\omega/2\pi \approx 1.2$ kHz. The third trace, from a probe on the HFS, does not display this frequency peak. This is consistent with the idea that the favorable magnetic curvature on the HFS stabilizes the fluctuations to long wavelengths. Over the connection lengths represented, $20 \text{ m} \leq L_c \leq 50 \text{ m}$, the location of the peak in the power spectrum tends to increase in frequency with an average value of $f = 1.3 \pm 0.3$ kHz. To obtain wave-number and phase velocity information, we employ cross-spectral analysis techniques described in Ref. 20.

A typical cross spectrum for the range of connection lengths examined here is shown in Fig. 5(b). Taking the cross spectrum of two vertically separated probes on the LFS with $\Delta z = 0.1$ m, we determine that in this range of connection lengths the LFS fluctuations possess associated wave numbers $k_z = \alpha_{nm}'(f)/\Delta z = 7.5 \pm 2.9 \text{ m}^{-1}$, where $\alpha_{nm}'(f)$ is the cross phase between the two spatially separated probes collecting ion saturation currents. The corresponding poloidal wavelengths are $\lambda_z = 1.0 \pm 0.4$ m. Because the cross phase is directly related to the wave number, it is equivalent to the experimental determination of the dispersion relation, $k_z(\omega)$, which, as seen in Fig. 5(b), has linear structure, $\omega = v k_z$, in

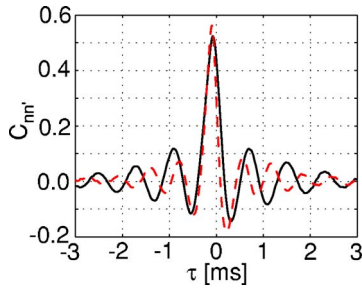


FIG. 6. Poloidal cross-correlation functions between two sets of probes, $\Delta z=9$ cm, located at radial positions on the LFS $r=122$ cm (dashed red) and $r=130$ cm (solid black).

accord with drift waves. The cross phase is shifted to increasing positive values for increasing frequencies, indicating that the fluctuation is propagating in the positive poloidal direction. The phase velocity is obtained by calculating the slope, s , of a linear fit to the data points. For the phase velocity we obtain $v = \omega/k_z = 2\pi f \Delta z / \alpha_{n\phi} = 2\pi \Delta z / s = 1.2 \pm 0.2$ km/s. The cross coherency provides a frequency-resolved measure of the correlation between the two probe signals while ignoring their phase information. We note here that these signals are partially coherent, possessing a high level of cross coherency at lower frequencies, $\gamma_{n\phi} \approx 75\%$. The wave frequency, $\omega = 2\pi \times 1.3$ kHz $\approx 8 \times 10^3$ s $^{-1}$, corresponds to an axial mode number of $m = 2Hk_z / \pi = 2\omega H / v_d \pi \approx 5$. Thus, we observe a partially coherent mode we expect to be unstable with $k_z \rho_s = 0.15 \pm 0.06$. Further evidence is provided by looking at poloidal cross-correlation functions for similar sets of probes. These are shown in Fig. 6, displaying oscillations at a dominant frequency of $f = 1.2 \pm 0.3$ kHz and a peak correlation value of at least 50%. The quick decay of the oscillation, on the order of 1 ms, indicates that the corresponding frequency peak has a width of ~ 200 – 300 Hz, which is characteristic of turbulent broadening of the fluctuations. The cross-correlation function is more reliable in determining the direction of propagation than the cross-phase analysis. In this case the cross correlation is computed between a pair of poloidally separated probes, in which the upper probe is used as a reference signal. The negative time shift of the $\tau=0$ axis indicates that the bottom probe sees the signal before the top probe, demonstrating that the fluctuation is experimentally measured in the lab frame to be propagating in the upward, or $+z$, direction. The measured phase velocity is $v = \Delta z / \Delta \tau_0 = 1.0 \pm 0.2$ km/s, consistent with the results from the cross-spectral analysis. Other modes with both higher and lower frequencies and different characteristics become apparent at longer connection lengths; however, these results are currently beyond the scope of this study.

Over the values of pitch considered with connection lengths between $20 \text{ m} \leq L_c \leq 50 \text{ m}$, the vertical wave number has a range $k_z \approx 7.5 \pm 2.9 \text{ m}^{-1}$. Estimating the range of parallel wave numbers, we obtain $k_{\parallel} = k_z B_z / B \approx 5.8 \times 10^{-3} \pm 1.2 \times 10^{-3} \text{ m}^{-1}$ for values of $0.0006 \leq B_z / B \leq 0.001$. This leads to a parallel wavelength on the order of $\lambda_{\parallel} \approx 1$ km, which is much larger than the connection lengths considered in these experiments. Thus, the relevant parallel length scale in this operating regime is the connection length; using the electron

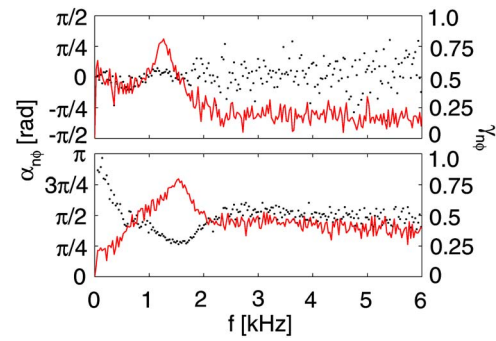


FIG. 7. Cross coherency, $\gamma_{n\phi}$ (solid red), and cross phase, $\alpha_{n\phi}$ (dotted black), between adjacent probes measuring ion saturation and floating potential, respectively. The upper plot corresponds to a probe pair 8 cm radially outward from the density peak on the LFS. The lower plot corresponds to a probe pair 26 cm radially outward from the density peak on the LFS.

thermal velocity $v_{Te} \approx 1.3 \times 10^6$ m/s, we then estimate the electron transit time along the field lines $L_c / v_{Te} \approx 2 \times 10^{-5}$ s. Note that the electron mean-free path is $\lambda_{en} \geq 300$ m for argon neutrals and $\lambda_{ei} \geq 10$ m for argon ions, so that electron-ion collisions dominate and the mean-free path is on the same order as the connection length in this operating regime for the device.

Because the time scale given by the electron transit time along the field lines is more than an order of magnitude faster than the wave frequency or $k_{\parallel} v_{Te} \gg \omega$, it is a good approximation to assume that the electrons maintain a local Maxwell-Boltzmann distribution. Thus, it would be expected that the resistivity creates a phase difference between the density and potential fluctuations which then produces a net radial particle transport (see Ref. 21). The measured cross phase between density and floating potential probes, $\alpha_{n\phi}$, is shown in Fig. 7. The cross-spectral analysis is performed between neighboring ion saturation and floating potential probes. The probe pair near the density peak (upper plot) is on the steep part of the LFS density gradient, whereas the probe pair on the outward edge of the plasma (lower plot) is located in a relatively flat region of the gradient. In this case the pair position relative to the density peak is adjusted by changing the toroidal magnetic field and moving the resonance either closer to or further away from the probes. The distance between the two pairs is $\Delta r = 18$ cm. For both cases the cross-coherency peaks with values of $\gamma_{n\phi} \sim 0.75$, indicating that the density and potential are highly correlated at the observed dominant fluctuation spectrum frequencies. In the case of the plasma edge, however, the coherency spectrum remains fairly high, $\gamma_{n\phi} \sim 0.5$, and broad, signifying that the density and floating potential fluctuations remain partially coherent for a greater range of frequencies on the LFS tail of the gradient. Near the peak the density and potential appear to be in phase as seen in the upper portion of Fig. 7. On the edge they are $\pi/2$ out of phase, indicating that either dissipation is playing a part or that another mechanism not investigated here becomes important in this region of the gradient. A more detailed analysis of the radial particle transport properties associated with these fluctuations and their phase difference must be undertaken.

By looking at the radial cross-correlation function, Fig.

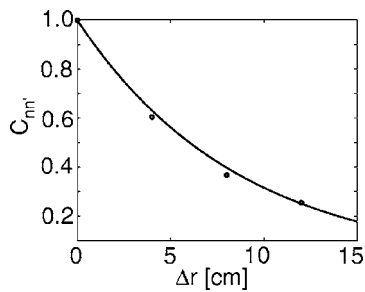


FIG. 8. Radial cross-correlation function between sets of probes with $\Delta z = 0$ cm and $\Delta r = 0, 4, 8, 12$ cm.

8, we can determine the radial length scale of the turbulence. Here, we have taken a set of radially spaced probe pairs ranging from $\Delta r = 0$ cm to $\Delta r = 12$ cm and plotted the maximum value of correlation function versus radial separation. The points were then fitted to the function $e^{-\Delta r/\lambda}$, where $\lambda = 8.67$ cm decay length of the radial correlation. Note that this scale length is consistent with the density gradient scale length of $L_n \approx 10$ cm. Thus, we do not expect fluctuation measurements made at a radial separation of greater than ~ 10 cm to have a high degree of correlation, and the radial extent of the fluctuations observed is bounded by this distance. It is also important to note that the turbulence length scale is an order of magnitude smaller than the radius of the machine, $\Delta r = 1$ m.

V. CONCLUSIONS

We have shown for the Helimak that the density gradient driven resistive drift wave turbulence dominates the growth rate at short wavelengths, and a resistive drift wave version of the Rayleigh-Taylor interchange instability dominates the spectrum at long wavelengths. A linear dispersion relation has been derived for the Helimak which is consistent with the experimental measurements of density and floating potential fluctuations.

The magnetic curvature radius R_c of the field lines is equal to the radius r of the local position from the symmetry axis in the system. Due to the negligible plasma beta, the gradient- B drift contribution equals that of the curvature drift for the hot electron component, and these combine to give the charge separating drift frequency $\omega_D = 2k_z T_e / eBR$.

In Sec. III C we have shown that the growth rate at short wavelengths is proportional to the square of the density gradient, and that at long wavelengths it is proportional to the product of the density gradient and magnetic field line curvature. The transition occurs at roughly $k_z \rho_s = (2L_n/R_c)^{1/2}$ to the Rayleigh-Taylor growth rate $\gamma_{\text{MHD}} = (2T_e/m_i L_n R_c)^{1/2}$ in the unfavorable curvature side by the adiabatic electron shielding. Note that the growth rate is proportional to the resistivity in the drift wave regime.

Thus, we expect and see in the experiment that there are large-amplitude drift wave fluctuations on the low field side of the density profile where the fictitious gravity due to the magnetic curvature is pointing down the density gradient. On the high field side of the maximum of the density profile the curvature is pointing up the density gradient so the long

wavelengths are stable. Only the shortest wavelength part of the spectrum can be unstable on the inside of the maximum of the density gradient profile.

The drift wave modes adjust themselves to have the longest parallel wavelength possible within the geometry. For low helical pitch the parallel wavelength can reach the limiting value of $k_{\parallel} = \omega/v_e$, where the thermal electrons resonate with the waves. This is the region of maximum growth rate for the drift waves. As the helical pitch becomes stronger the parallel wavelength becomes shorter and the growth rate decreases. This trend is seen in the experiment as shown in Fig. 4(b)

In Fig. 5(a) we show the power spectrum of the density fluctuation on the outside of the density profile in the region where the density gradient is near its maximum value. Here, the dominant mode is at $f_{\text{max}} = 1.2$ kHz, which corresponds to a vertical mode number of $m = 5$ and the associated wave number $k_z = 7.5\text{m}^{-1}$. The diamagnetic drift velocity is $v_{de} = T_e/eBL_n = 1$ km/s and the fractional shift of the frequency down from $\omega_{se} = k_z v_{de}$ due to ω_{De} is given by $2L_{ne}/R_c = 0.2$.

While the shortest wavelengths have a growth rate proportional to the square of the density gradient, the saturation level of these waves is low. The dominant part of the fluctuation spectrum is from the density gradient times the effective gravity from magnetic curvature pointing down the density gradient. The instability here may also be described as arising from the effective buoyancy of expanding density blobs in the fictitious gravity created by the curvature and gradient- B drifts of the electrons. The ions play almost no role except in neutralizing the waves in the electron fluid due to their heavy mass and cold temperature. Thus, the laboratory with the curved magnetic fields provides a method of directly simulating the role of gravity driven plasma modes on the surface of the sun and other stars.

Other modes that can be excited and will be studied in future experiments are the Kelvin Helmholtz modes and the fast MHD interchange modes.

ACKNOWLEDGMENTS

The work was supported under the U.S. Department of Energy Contract DE-FG02-04ER 54742 and the National Science Foundation.

¹N. D'Angelo and R. W. Motley, Phys. Fluids **6**, 422 (1963).

²F. F. Chen, Phys. Rev. Lett. **15**, 381 (1965).

³F. F. Chen, Phys. Fluids **8**, 752 (1965).

⁴F. F. Chen, Phys. Fluids **9**, 965 (1966).

⁵F. F. Chen, Phys. Fluids **10**, 1647 (1967).

⁶H. W. Hendel, T. K. Chu, and T. A. Politzer, Phys. Fluids **11**, 2426 (1968).

⁷F. L. Hinton and C. W. Horton, Jr., Phys. Fluids **14**, 116 (1971).

⁸D. Bohm, E. H. S. Massey, H. S. W. Burhop, and R. W. Williams, *The Characteristics of Electrical Discharges in Magnetic Fields* (McGraw-Hill, New York, 1949).

⁹W. Horton, Rev. Mod. Phys. **71**, 735 (1999).

¹⁰V. V. Parail, G. V. Pereverzev, and I. A. Vojtsekhovich, in "Proceedings of the IAEA Conference on Plasma Physics and Controlled Thermonuclear Fusion," London, 1985, Vol. I, p. 605.

¹¹E. D. Zimmerman and S. C. Luckhardt, J. Fusion Energy **12**, 289 (1993).

¹²S. Luckhardt, "The Helimak: A one dimensional toroidal plasma system," Technical Report, University of California, San Diego, 1999; <http://orion.ph.utexas.edu/~starpower>.

- ¹³S. H. Müller, A. Fasoli, B. Labit, M. McGrath, M. Podesta, and F. M. Poli, Phys. Rev. Lett. **93**, 165003 (2004).
- ¹⁴K. Rypdal and S. Ratynskaia, Phys. Rev. Lett. **94**, 225002 (2005).
- ¹⁵R. Dahlburg, Jean C. Perez, and W. Horton (unpublished).
- ¹⁶S. I. Braginskii, Rev. Plasma Phys. **1**, 205 (1965).
- ¹⁷S. T. Tsai, F. W. Perkins, and T. H. Stix, Phys. Fluids **13**, 2108 (1970).
- ¹⁸W. Horton and R. K. Varma, Phys. Fluids **15**, 620 (1972).
- ¹⁹A. Hasegawa and M. Wakatani, Phys. Rev. Lett. **50**, 682 (1983).
- ²⁰D. E. Smith and E. J. Powers, Phys. Fluids **16**, 1373 (1973).
- ²¹E. J. Powers, Nucl. Fusion **14**, 749 (1974).